



Sensible heat flux assessment in a complex coastal-mountain urban area in the metropolitan area of Rio de Janeiro, Brazil

Rafael João Sampaio¹ · Daniel Andres Rodriguez¹ · Celso Von Randow² · Fabricio Polifke da Silva¹ · Afonso Augusto Magalhães de Araújo³ · Otto Corrêa Rotunno Filho¹

Received: 21 June 2020 / Accepted: 9 June 2021 / Published online: 26 June 2021
© The Author(s), under exclusive licence to Springer-Verlag GmbH Austria, part of Springer Nature 2021

Abstract

Obtaining accurate estimates of surface-atmosphere energy exchanges and improved comprehension of the mechanisms generating turbulent fluxes over non-uniform landscapes are both challenging goals and essential for validating numerical weather forecasting modeling. In this work, a large-aperture scintillometer (LAS) was deployed to evaluate the effect of mesoscale sea and valley breezes with respect to diurnal sensible heat flux (H) variability over an urban area close to a coastal bay near the metropolitan area of Rio de Janeiro (MARJ) during the austral summer of 2017–2018 time span. The region is characterized by a densely urbanized environment, surrounded by mountainous relief and bounded by a large ocean bay. The transmitter and the receiver of the LAS system were installed 1955 m apart. Diurnal cycle was divided into four periods according to the local time: dawn (00 a.m. to 6 a.m.), morning (6 a.m. to 12 a.m.), afternoon (12 a.m. to 6 p.m.), and night (6 p.m. to 00 a.m.). The results demonstrated the sensitivity of the LAS to record variations in H over the course of the day, taking into account the corresponding sea and valley breezes and the relative humidity variability. During the morning, when valley breezes are predominant, footprint area shrinks to its smallest size, encompassing an area of approximately 2 km². On the other side, during afternoon and night time periods, during afternoon and night time periods, the presence of sea breeze jointly with a densely urbanized continental area contribute to promote significant changes in the footprint area ranging from 2.05 to 5.38 km². The effects of topography are also well captured in the diurnal H cycle once sunset and corresponding shading in the late afternoon abruptly reduces heat-sensible flux. Diurnal variations in footprint shape and area lead to modifications in terms of the mode each type of urban surface will contribute to H , increasing the influence of anthropogenic elements in afternoon and early evening. Complementarily, it is noteworthy to mention that a sensitivity test was performed to assess uncertainties in H estimates for the free convection method, which requires the estimation of an empirical constant b . Variations in this constant introduce larger dispersion in H estimates than potential errors in LAS effective height (Z_{eff}) estimations or temperature measurements. These last results highlight the importance of conducting further evaluations as the one pursued in this study to more rigorously validate the outputs of numerical mesoscale and local hydrometeorological models and remotely sensed products.

Responsible Editor: Silvia Trini Castelli.

✉ Rafael João Sampaio
samprafael@gmail.com

¹ Laboratório de Recursos Hídricos E Meio Ambiente (LABH2O), Programa de Engenharia Civil, COPPE, Universidade Federal do Rio de Janeiro, Av. Horácio Macedo, 2030, Rio de Janeiro 21941-450, Brazil

² Centro de Ciência do Sistema Terrestre (CCST), Instituto Nacional de Pesquisas Espaciais (INPE), Av. dos Astronautas 1758, São José dos Campos 12227-010, Brazil

³ Laboratório de Recursos Hídricos e Meio Ambiente (LABH2O), Departamento de Recursos Hídricos e Meio Ambiente, Escola Politécnica, Universidade Federal do Rio de Janeiro, Athos da Silveira Ramos, 149, Rio de Janeiro 21941-909, Brazil

1 Introduction

Sensible heat flux (H , Wm^{-2}) is an essential component of surface-atmosphere energy exchanges in urban areas due to relative lack of moisture and vegetation compared to non-urban environments (Crawford et al. 2018). Urban systems are usually characterized by higher Bowen ratios, with energy partitioning trending towards higher sensible than latent heat flux (Oke 1987) and large anthropogenic heat input largely influencing sensible heat fluxes (Iamarino et al. 2012). In addition, in coastal-mountainous urban areas, sea breezes (Pigeon et al. 2007; Anjos and Lopes 2019) and valley breezes (Román-Cascón et al. 2015) could increase the importance of heat storage and its diurnal variability in urban surfaces (Haeger-Eugensson 1999; Pigeon et al. 2007; Anjos and Lopes 2019).

The study of surface energy balance (SEB) in urban areas faces challenges due to the heterogeneity of the terrain. The vertical structure of the atmosphere above urban areas is influenced by roughness generated by individual elements (Pigeon et al. 2007; Oke et al. 2017), such that the concentration and height of the buildings turn out to be the main factors for the definition of roughness classes (Oke 2004). Heat storage through the anthropogenic component of SEB (Stull 1988) causes the atmosphere to change over time. Once the air over urban areas becomes warmer than the surrounding atmosphere, this atmospheric condition creates the so-called urban heat islands (Papangelis et al. 2012; Zang and Zhang 2014; Zeng and Gao 2017; Peres 2018; Giannaros et al. 2018). As the development of urban heat islands is related to the local surface boundary layer structure (Masson 2000), anthropogenic activities introduce an additional convection force (Vázquez et al. 2018).

In coastal cities, differences in energy balances between water and land surfaces cause the circulation of breezes (Oke 1987). The influence of sea breeze generates variations in the height of the boundary layer, as showed by Mestayer et al. (2005) in a field campaign in Marseille, France, and by De Tomasi et al. (2017) in Lecce, Italy. Vázquez et al. (2018) studied the coastal boundary layer in New York and highlighted that the interaction between the highly convective urban surface layer and the marine boundary layer led to the development of an internal boundary layer. Although many studies have investigated the evolution of the boundary layers at coastal sites (Melas and Kambezidis 1992; Sicard et al. 2006; Boselli et al. 2009; Papangelis et al. 2012; Giannaros et al. 2018), more effort and sustained observations are necessary to improve the predictability of the boundary layer in coastal-urban environments (Vázquez et al. 2018). This is especially true for environments with complex topography, where valley breezes also occur (Goldreich et al. 1986; Naor et al. 2017).

Sensible heat flux (H) is an important element for the modeling of dynamic urban atmosphere processes and turbulent surface energy fluxes. These fluxes play a key role in regulating the energy balance of the atmosphere, which in turn drives atmospheric circulation (Chehbouni et al. 1999; Lee 2015). The eddy covariance (EC) approach is commonly used in studies to estimate in-situ H , as well as for the numerical modeling of land-atmosphere heat flux exchanges (Ingwersen et al. 2011; Zhao et al. 2014; Imukova et al. 2015; Liu et al. 2017; Sun et al. 2017). The large-aperture scintillometer (LAS) is an alternative for collecting H data that has the advantage of aggregating larger spatial scales than the EC approach, which can then be compared to satellite images and numerical models (Klessl et al. 2009; Al-Gaadi et al. 2016; Valayamkunnath et al. 2018). The LAS estimates turbulent fluxes through Monin-Obukhov similarity theory (MOST) using the refractive index of air (C_n^2), as measured by scintillations acquired in the infrared at 880 nm wavelength, as a structural parameter (Ezzahar et al. 2007a, b; Zhao et al. 2018).

Previous studies have shown LAS has satisfactory performance in deriving H levels compared to flux measurement using EC (Klessl et al. 2009; Xu et al. 2013, 2017; Liu et al. 2013; Yee et al. 2015; Zhao et al. 2018). Such application has been explored in different field campaigns conducted in sites with varied land covers, such as grasslands (Watts et al. 2000; Hemakumara et al. 2003; Von Randow et al. 2012), tropical forests (Von Randow et al. 2008), agricultural land (Ezzahar et al. 2007a, b; Minacapilli et al. 2016), urban areas (Lagouarde et al. 2005; Zhang et al. 2014; Ward et al. 2014; Zieliński et al. 2018) and water bodies (Lee et al. 2015; Lee 2015). However, few studies use the scintillometer in urban coastal environment.

This study examines diurnal variations in sensible heat flux (as measured by an LAS) over an urban island located inside a coastal bay during summer time, and addresses the contribution of scintillometry for this understanding. It is structured as follows: Sect. 2 provides reports on the study site and experiment conducted as well as the basic theoretical principles grounding the determination of H by a scintillometer system; Sect. 3 provides results and corresponding discussion; and Sect. 4 presents concluding remarks about the research study.

2 Methodology and dataset

2.1 Site description and experimental setup

The Fundão Island is an urban island located in the Metropolitan Area of Rio de Janeiro (MARJ), close to Guanabara Bay. The island has an area of approximately 6 km^2 , with about 30% of its surface occupied by buildings, pavements

and urban facilities that make up the campus of the Federal University of Rio de Janeiro (UFRJ). The remaining extent of the island is covered by grassland and small areas of mangrove. Total population inflows and outflows on campus add up to approximately sixty thousand inhabitants. The western and southern parts of the Fundão Island are both surrounded by densely populated urban areas. To the north is the Governador Island, which is the site of the Tom Jobim Airport (Fig. 1). The Guanabara Bay spreads for approximately 30 km along the north–south direction and 28 km in the west–east direction (Soares-Gomes et al. 2016). The coastal bay line is dominated by a mountainous relief. The urban area of the city of Rio de Janeiro is mostly situated between two massifs, namely Tijuca and Pedra Branca, (maximum heights 1021.00 m and 1024.00 m, respectively). These massifs act as barriers for southwestern winds, dampening out air circulation on the areas behind them and forcing air flow into what is called wind corridors (Zeri et al. 2011).

According to the Köppen climate classification, the region's climate corresponds to the Aw class, characterized by dry and cool winters and wet and rainy summers (Zeri et al. 2011). Guanabara Bay is influenced by thermal wind regimes (sea/land breezes). In particular, east-southeastern winds are associated with sea breeze, while northwestern winds are influenced by land breeze (Giannaros et al. 2018). The South Atlantic Convergence Zone (SACZ) also plays an important role in local weather. The SACZ is an elongated and persistent band of convection that usually occurs during the summer season (December–March) and

frequently extends from the Amazon region to the Brazilian south and southeast offshore and Atlantic Ocean (Villela 2018).

Sensible heat flux (H) was measured via a BLS 450 large-aperture scintillometer (LAS) (Scintec AG, Rottenburg, Germany) deployed over a 1955 m path over the top of two buildings at 45 m and 85 m height—namely the University Hospital (HU, 22°50'33.77"S/43°14'18.18"W) and Technological Center (CT, 22°51'32.53"S/43°13'51.08"W), respectively. The effective height is 59.44 m, accordingly to Hartogensis et al. (2003). The LAS operates at the 880 nm wavelength and its lens has a 145 mm aperture diameter. Performance assessments of the LAS can be further reviewed in Xu et al. (2013), Sun et al. (2016) and Xu et al. (2017). Output data are stored at 5-min intervals obtained from averaging over 10 samples, each collected along 30-s time periods.

Temperature, relative air humidity, and solar radiation data were collected by a weather station located in the Institute of Geosciences (IGEO) of the Federal University of Rio de Janeiro on Fundão Island, (− 22° 51'26.45"/− 43°14'07.31"), 305 m away from the LAS receiver. The data collection platform was programmed to record data every 10 min from sensors installed at 1.5–2.0 m in height. Wind speed and direction data were obtained at the Galeão International Airport weather station (SBGL) in METAR format, 3900 m away from the transmitter.

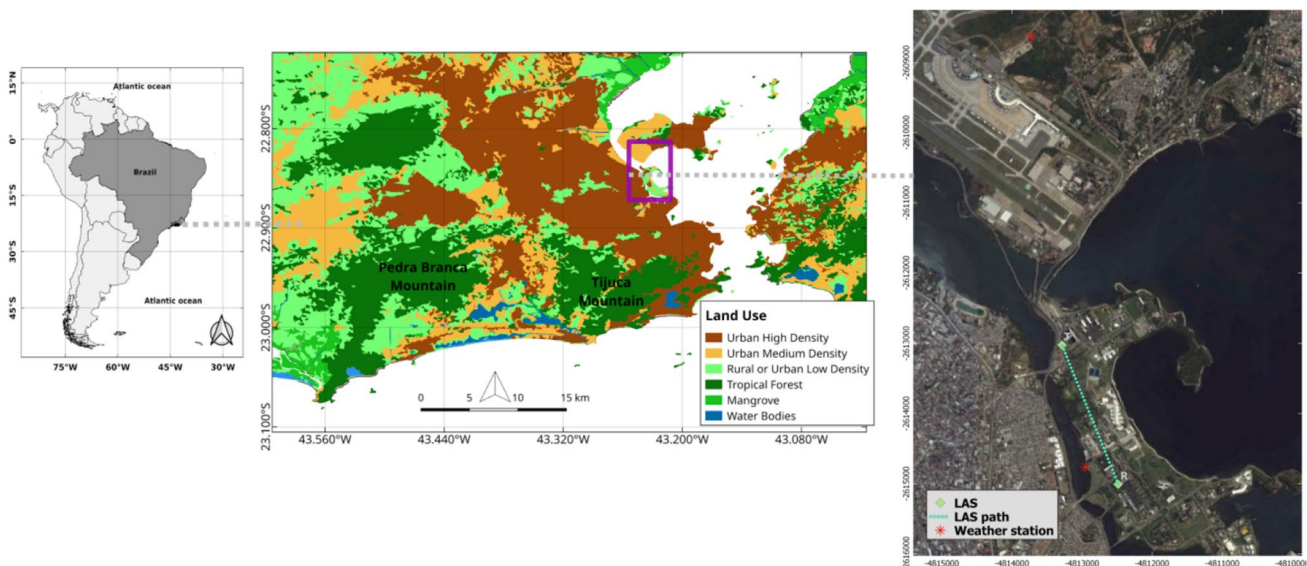


Fig. 1 Section of the municipality of Rio de Janeiro showing the measurement sites at Galeão Airport (Governador Island) and at the UFRJ campus, both with their corresponding weather stations (red stars). The latter is located at the UFRJ's University City—Fundão

Island, depicted here by a transect between two spots, namely University Hospital (HU) (T—Transmitter) and Technological Center (CT) (R—Receiver) (Source: Google Maps) (left)

2.2 Scintillation method

The estimation of H via scintillometry is based on measuring fluctuations in the intensity of a light beam, particularly the part of the electromagnetic spectrum that covers the visible and infrared wavelength range, which propagates through tens to hundreds of meters between the two modules of the scintillometer (Thiermann and Grassl 1992). As we can solve the propagation of a spherical wave through a medium with fluctuations in the refractive index, it is possible then to relate the variance in the fluctuations intensity logarithm (σ_{\ln}^2) and the refractive index structure parameter referred to as C_n^2 (Tatarskiĭ 1961; Hill and Lataitis 1989). The C_n^2 equation for an LAS with equal aperture diameters for transmitter and receiver was described by Wang et al. (1978) as:

$$C_n^2 = 1.12 \sigma_{\ln}^2 D^{\frac{7}{3}} L^{-3}, \quad (1)$$

where D is the aperture diameter, and L is the path length.

The refractive index of a gas depends on its composition and state variables, namely pressure and temperature. Given the fact that water vapour is by far the most important component with for the evaluation of air under atmospheric conditions, the composition of that air parcel can be described in terms of a constant composition of dry air and a varying concentration of water vapour, notably in terms of water vapour pressure or specific humidity (Moene 2003). Therefore, C_n^2 can be represented in terms of the air temperature C_t^2 and air humidity C_q^2 structural parameters. On the other hand, air temperature is a greater contributor to fluctuations in the wavelengths along the visible and the near infrared bands of the electromagnetic spectrum in which the scintillator usually operates (Wesely 1976). In this paper, the wavelength λ adopted was 880 nm. The fluctuations caused by air humidity dominate the portion of the electromagnetic spectrum associated with the microwave range (Tatarskiĭ 1961; Yee et al. 2015). Thus, C_t^2 can be represented as a function of C_n^2 , leading to Eq. 2, as proposed by Wesely (1976):

$$C_t^2 C_n^2 \left(\frac{T^2}{-0.7810^2 P} \right)^2 \left(1 + \frac{0.03}{Bo} \right)^{-2}, \quad (2)$$

where T is air temperature (K), P is atmospheric pressure (Pa), and Bo is the Bowen ratio. The error generated by neglecting the influence of air humidity is compensated by Bowen's ratio (Moene 2003).

In unstable free convection conditions with $\xi \rightarrow -\infty$, H can be estimated directly from C_t^2 by means of the following equation:

$$H_{free} = -\rho c_p b z_{eff} \left(\frac{g}{T_a} \right)^{\frac{1}{2}} (C_t^2)^{\frac{3}{4}}, \quad (3)$$

where C_p represents heat capacity ($\text{J kg}^{-1} \text{K}^{-1}$), ρ is the air density (kg m^{-3}), b is a constant estimated empirically ($b = c_1^{-3/4} k c_2^{1/2}$) and c_1 and c_2 are empirical constants. De Bruin, (1995) used $b=0.57$, Andreas (1988) used $b=0.474$, and Kohsiek (1982) used $b=0.55$. The value is strongly dependent on the chosen parameterization (Lagouarde et al. 2005). For this work, we adopted $b=0.57$ (De Bruin et al. 1995).

Free convection approaches have been shown to generate reasonable behaviors under unstable conditions, with results closer to those obtained from the mixed convection approach (Lagouarde et al. 2005; Zieliński et al. 2013). On the other hand, under near-neutral conditions, there is an underestimation of heat fluxes, which could be associated with uncertainties in the estimation of z_{eff} (Lagouarde et al. 2005; Crawford et al. 2017).

When deriving H from scintillometer measurements, stability can be employed to determine whether the use of specific free convection assumptions is appropriate. Comparisons between the 'free convection' and 'mixed convection' solutions with the use of similarity theory functions to estimate H indicate good agreement during unstable conditions (Lagouarde et al. 2005; Zieliński et al. 2013). Overall, the free convection solution tends to underestimate H during near-neutral conditions, since it does not take mechanical turbulence into account (Sect. 2.3). However, the free convection solution relies on fewer meteorological variables and their associated uncertainties, which is an advantage over the other methods (Lagouarde et al. 2005).

2.3 Data processing

The LAS system collected observational data for 50 days during the 2017–2018 summer time, more specifically from December 16, 2017 to February 6, 2018. To ensure the quality of the data measured by the LAS system, we discarded data collected along time periods in which rainfall took place and when C_n^2 values were above a saturation threshold established at $2.7 \times 10^{-11} \text{ m}^{-2/3}$ (Ochs and Hill 1982; Zhao et al. 2018). Implausible values of H , namely lower than -100 Wm^{-2} or higher than 600 Wm^{-2} (Zhao et al. 2018), were also discarded. In total, 14 days (16–22 December, 2017 and 16–22 January, 2018) were finally selected. Stable conditions were defined to be the time periods when net radiation (R_n) was lower than 50 Wm^{-2} , while periods in which R_n was higher than 50 Wm^{-2} were considered to represent unstable conditions (Samain et al. 2012).

2.4 Three-dimensional LAS footprint modeling

The footprint model is a useful tool to evaluate the area of upwind contribution to surface fluxes. This model estimates the per-unit flux contribution of each part of the upwind area

(Hoedjes et al. 2007; Sun et al. 2016). The source strength function is expressed by the following equation:

$$F(x, y, z_m) = \int_{-\infty}^{\infty} \int_{-\infty}^x S_0(x', y') f(x', y', x - x', z_m) dx' dy', \quad (4)$$

where x represents downwind distance from the measurement location, y is the crosswind distance from the centerline, z_m is the measurement height, and $F(x, y, z_m)$ is the spatial distribution of upwind surface flux $S_0(x, y)$. We used the approach proposed by Kormann and Meixner (2000) and Liu et al. (2011) for unstable conditions. This method is based on an Eulerian analytic flux footprint model, which is here implemented to obtain the flux footprint of a single point vertical flux measurement $f(x, y, z_m)$ given by the expression:

$$f(x, y, z_m) = D_y(x, y) f_y(x, z_m), \quad (5)$$

where z_m represents the measurement height (m), x is the downwind distance pointing against the average horizontal wind direction, y is the crosswind distance, z_m is the measurement height, $f_y(x, z_m)$ is the crosswind integrated footprint, and $D_y(x, y)$ is the Gaussian crosswind distribution function of the lateral dispersion. The LAS footprint function is combined with a bell-shaped weighting function that defines the contribution along the scintillometer path (Meijninger et al. 2002). It should be noted that f_{LAS} describes the source strength as:

$$f_{LAS} = f(x, y, z_m) * W(x, y), \quad (6)$$

where $W(x, y)$ represents the weight function of the LAS, as reported by Hartogensis et al. (2003). The operator $*$ expresses a convolution between both functions on the right side of Eq. 6. In this study, the footprint area for H fluxes was obtained for each sub-daily period, considering unstable meteorological conditions with $z_{eff}/L = 0.02$ and $u_{star} = 0.8$.

Scintillometer turbulent flux measurements are influenced by the distribution of wind directions and atmospheric stability, factors that change the orientation and shape of the source area. On a homogeneous surface, changes in the shape of the footprint would be irrelevant if the surface composition of heat sources and sinks remains the same. Nonetheless, surface variations in soil cover and heat sources and sinks can be of the same order of magnitude as the measurement length scales in urban environments, such that areas of varying sources should be taken into account (Crawford et al. 2017). Specifically for scintillometers, the Monin–Obukhov similarity theory (MOST) is unsuitable for measurements over urban and suburban surfaces, where wind flow is non-stationary and turbulence properties vary in space and time (Zhang and Zhang 2014).

Footprint models can be used to assist the analysis of observed fluxes to better describe and associate them with

the probable area of the surface that influenced the measurements. Even though some of the assumptions might be challenged by complex environments, footprint models have been used successfully in urban areas, provided that measurements are made at a height level for which the influences of individual obstacles or heterogeneities are averaged out (Ward et al. 2014). In this study, land use and land cover maps from the State Institute of the Environment of the Rio de Janeiro on a scale of 1:50,000, (available at <http://www.inea.rj.gov.br/>) were used to quantify the type of land cover that most contributes to each source area.

2.5 Uncertainty assessment

2.5.1 Sensitivity analysis of the measured sensible heat flux

Uncertainties related to the H free convection estimation method were evaluated. The sensitivity test was applied for the period from 16 to 22 December, 2018, considering stable and unstable conditions. For this analysis, we used the b constant values (Eq. 3) obtained by Andreas (1988) and Kohsiek (1982). Due to the importance of air temperature for the calculation of H , in particular for this free convection methodological approach, we evaluated the effect of a $\pm 10\%$ variation in input temperature to quantify the uncertainties related to the measurement of this variable. To determine this range, we used a reference average diurnal increase at 10-min time steps, which is the time step of temperature measurement.

Estimating H through the free convection method is also strongly influenced by z_{eff} (Hartogensis et al. 2003). The uncertainty in z_{eff} is caused by low measurement accuracy, dependence on effective height with atmospheric stability and surface heterogeneity (Ward et al. 2014). The WorldDEM data used to describe the topography of the region has a 12-m spatial resolution and an averaged vertical error of 7 m (Becek et al. 2016; AIRBUS 2015). Thus, variations of ± 7 m on z_{eff} were analyzed to quantify the uncertainties caused by the topographic elevation model used to obtain that variable.

2.5.2 Sensitivity analysis of the footprint models

Wind speed and direction largely control shape and area of the footprints. The uncertainties in the estimated source areas were investigated using numerical simulations of the wind field. We used the Weather Research and Forecast (WRF) model to simulate wind speed and direction, from which footprint areas for sensible heat in the area were also estimated. Uncertainties were assessed by comparing both simulated and measured based wind patterns and the associated area and shape of the footprint. It should be

noted that WRF is widely used in studies of local surface flow (Sun et al. 2017; Liu et al. 2018; Jiménez-Esteve et al. 2018). The model achieves relatively accurate performance in urban coastal regions (e.g., Lee et al. 2011; Giannaros et al. 2018). At the MARJ region, WRF has properly simulated atmospheric thermodynamic processes (Silva et al. 2017) and wind and air temperature fields (Giannaros et al. 2017; Dragaud et al. 2018; Paranhos et al. 2019). Giannaros et al. (2017) found mean bias errors of $\pm 0.5 \text{ ms}^{-1}$ and $\pm 16^\circ$ in the forecast of wind speed and direction, respectively, with the application of WRF over MARJ. Lee et al. (2011) showed similar results in simulations of direction and wind speed in a coastal region. Main model's limitations are associated with the numerical and physical configuration for the region of interest together with the resolution of the terrain data (Carvalho et al. 2014).

WRF version ARW-3.8 (Skamarock et al. 2008) has been developed in a cooperative effort coordinated by the National Center for Atmospheric Research (NCAR). It is a numerical weather prediction system designed to serve both operational forecasting and atmospheric research needs (De Tomasi et al. 2017). Given a proper experimental configuration, the WRF model has the capability to explicitly represent significant surface land-use heterogeneity over the field experiment region and to resolve associated land-surface physical (radiative/dynamic/hydrological) processes (Lee et al. 2015).

The WRF was configured with three nested domains, the first with 27 km of horizontal resolution, the second with 9 km and the third with 3 km. We configured the model using parameterizations used for Da Silva (2017) in the MARJ region. The model was applied with 27 vertical levels, with the highest level in 50 hPa, and 4 vertical soil levels. The physical parameterizations adopted used the Rapid Radiative Transfer Model for long-wave radiation (Mlawer et al. 1997), the WRF single-moment three-class microphysics scheme (Hong et al. 2004), the Dudhia short-wave radiation scheme (Dudhia 1989), the Revised MM5 Monin–Obukhov (Jiménez et al. 2012) for surface layer, the Unifed Noah land surface model (Tewari et al. 2007) and the Yon-Sei University Planetary Boundary Layer parameterization scheme (Hong et al. 2006). Initial and lateral boundary conditions retrieved from an analysis conducted using the Global Forecast System (GFS, <http://www.emc.ncep.noaa.gov/GFS/doc.php>) with 6-h intervals and horizontal resolution of $0.50^\circ \times 0.50^\circ$ were provided to the WRF model. Two numerical simulations were performed for both intervals studied, 16–22 December 2017 and 16–22 January 2018. Model output was obtained in 1-h intervals.

3 Results and discussion

3.1 Meteorological conditions

The austral summer months make up the rainy season of Rio de Janeiro, which is characterized by high air temperature and air humidity values. The measured average temperature for December 16–22, 2017 was 28.3°C , with a low and high of 21.8 and 37.3°C , respectively. Air specific humidity was 0.016 g g^{-1} . From 16–22 of January, 2018, recorded average air temperature was 28.8°C , with a low of 22.7°C and a high of 38.7°C . Averaged air specific humidity was 0.016 g g^{-1} . The weather was considered to be clear along the 14 days of the field experiment, without records of any rainfall. The highest diurnal variations in both air temperature and air specific humidity took place in December 17, 2017 and January 18, 2018, respectively (Fig. 2).

Data on diurnal variations of wind direction and speed, collected hourly, were analyzed in four sub-daily periods: dawn (00 a.m. to 6 a.m.), morning (6 a.m. to 12 a.m.), afternoon (12 a.m. to 6 p.m.), and night (6 p.m. to 00 a.m.). The wind rose of each time period shows the switch between sea breeze and land breeze regimes during the days of the experiment (Fig. 3). The northern (N) component of wind is characteristic of the land breeze (Júnior et al. 2013; Pimentel et al. 2014; Sobral et al. 2018), which occurs due to the mountainous relief that surrounds the Guanabara Bay (Fig. 1). Conversely, sea breeze is characterized by south-eastern (SE) wind (Júnior et al. 2018). During the dawn period (Fig. 3a), eastern (E), southeastern (SE) and western (W) winds are predominant. In the morning period, predominance changes to north (N) and to east (E) winds. During the afternoon, the prevailing wind direction switches to south-east (SE). The wind pattern shown during afternoon persists during the night period, with the same preponderance of southeast (SE) winds, but lower frequencies from the other directions. Sea breeze events occur most frequently during the afternoon and night, while the land breeze regime is more intense in the morning. Sea breeze events reach higher wind velocities than the ones found in valley breezes. This daily behavior is characteristic of the region (Junior et al. 2013; Pimentel et al. 2014; Júnior et al. 2018).

3.2 Footprint analysis

Our analysis shows that, for a selected length path of approximately 2 km, the area responsible for 95% of the contributions to the measured values varies from 2.05 to 5.38 km^2 . Variations in the magnitude of the area are

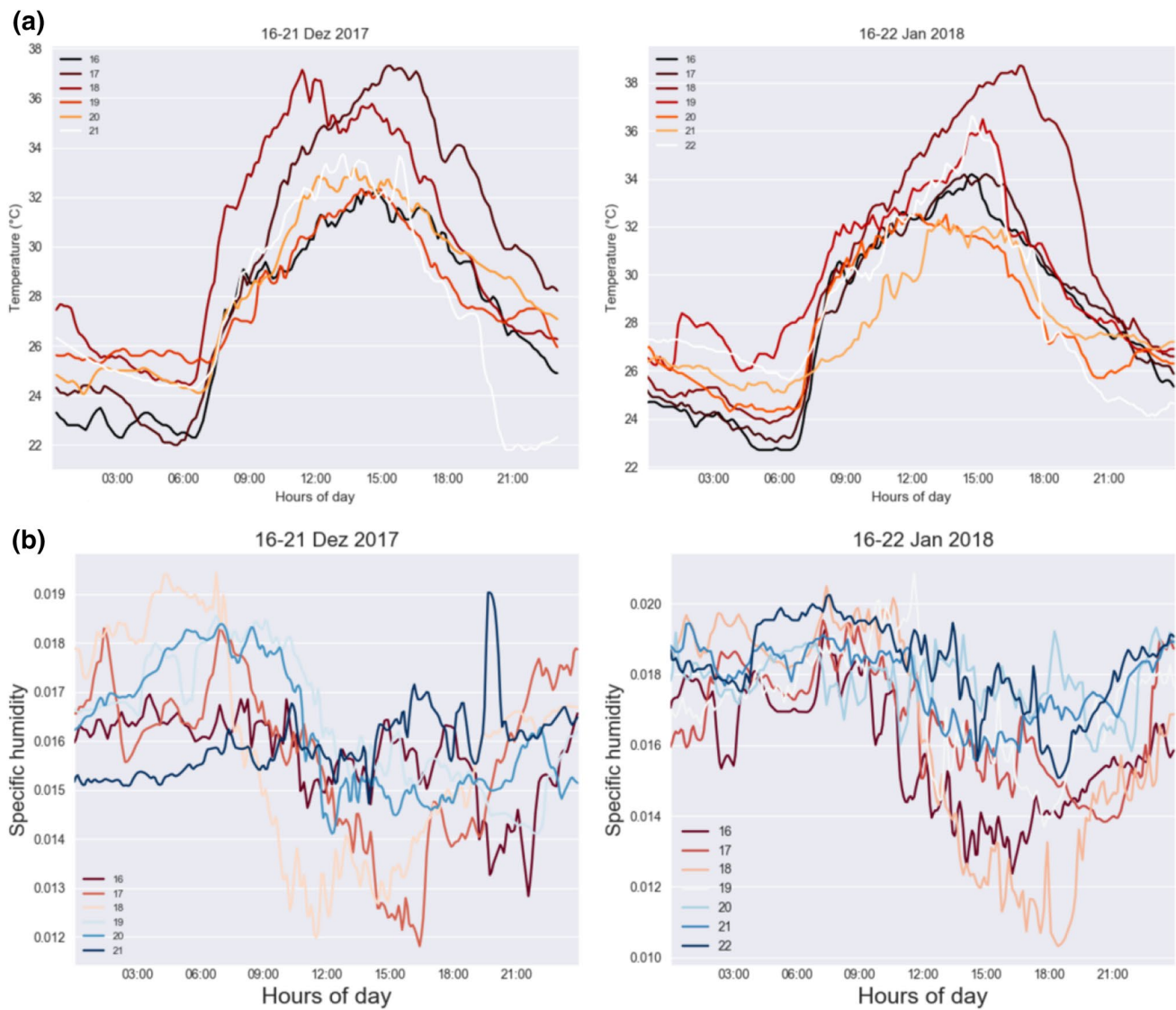


Fig. 2 Air temperature (Celsius degree) and air-specific humidity (g g^{-1}) data for December 16–21, 2017 and January 16–22, 2018

related to changes in wind speed and direction (Fig. 3). In the dawn and morning periods, low wind velocities reflected footprints of 2.78 and 2.05 km², respectively (Fig. 3a, b). The footprint extends mainly over the territory of the island, entering just a small portion into the continent and the Guanabara Bay. In the afternoon and night periods, sea breeze increased the source areas in the southern-eastern direction, reaching 3.63 km² and 5.38 km². The urban continental area was a greater contributor to H during these time periods compared to dawn and morning.

The variation in size and shape of the footprint also alters the land-cover that contributes to the values of H . In the dawn period, water surface and continental high-density urban occupation are the most important contributing factors to footprint, accounting for 30% and 29% thereof,

respectively (Fig. 4). In the morning, contribution from the continental high-density urban areas (18.85%) decreases, while there is an increase in the contribution of low-urban-density island areas (23.25%). In the afternoon, the absolute footprint area increases considerably. Water and low-density urban use also have the highest contribution rates (34.5% and 23.3%) during this period. At night, as the footprint has extended towards the urbanized continent, the contribution of high-density urban areas increased, reaching 33.4% of the footprint against 21% from water, 11% from medium-density urban areas and 20.3% from low-density urban areas.

These results suggest that urban surface influence measurement uncertainties have diurnal variation. Urban fraction contribution increased from 46.2 to 64.7% as variations from afternoon to night periods were examined (Fig. 4). This highlights the influence of breezes in shaping the footprint

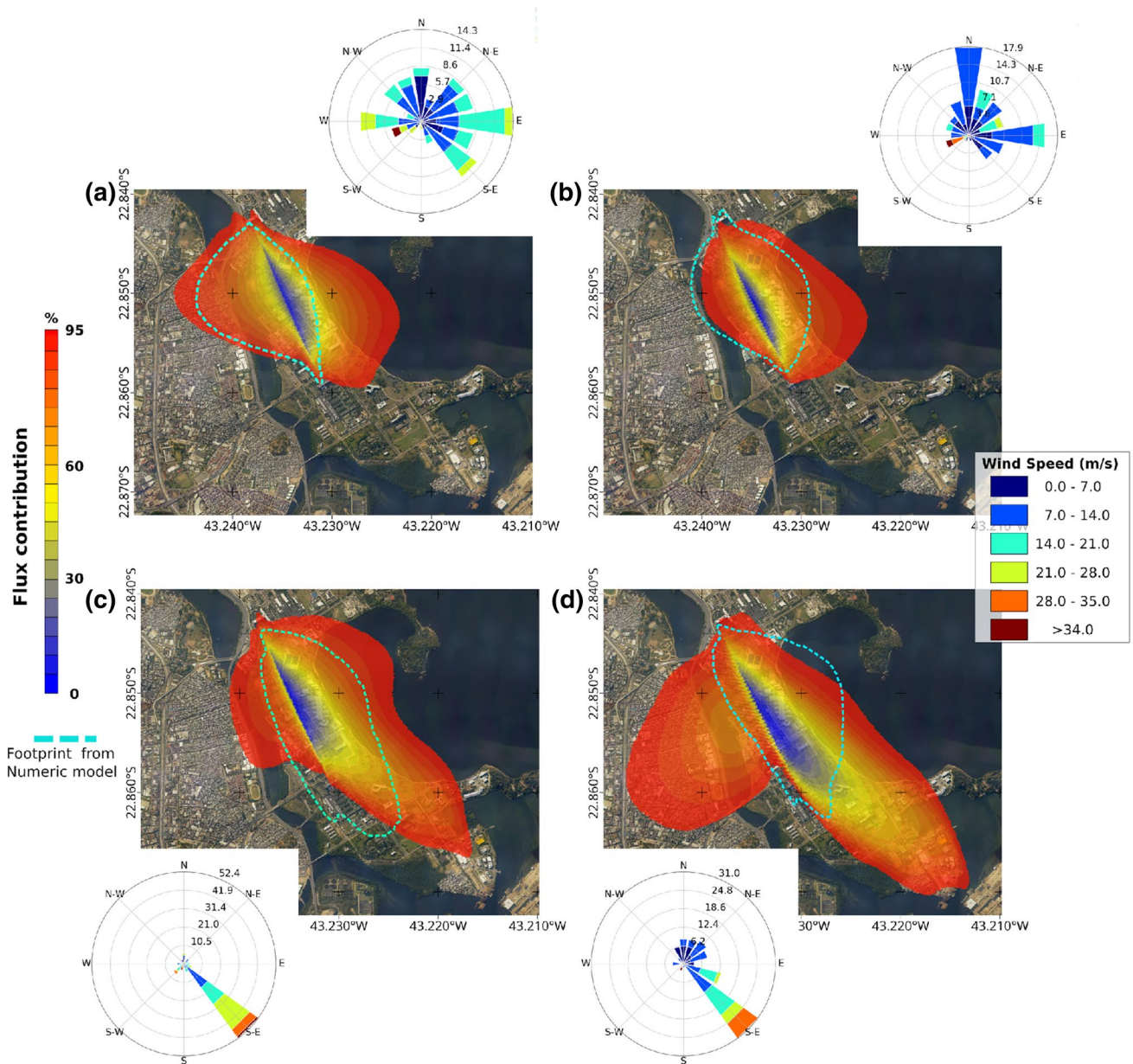


Fig. 3 Wind rose diagrams with the wind speed (ms^{-1}) frequency distribution broken down by wind direction, depicted for four time periods during the field experiment, and the corresponding footprint under each wind direction condition: **a** dawn (12 a.m. to 6 a.m., upper

left); **b** morning (6 a.m. to 12 p.m., upper right); **c** afternoon (12 p.m. to 6 p.m., lower left); **d** night (6 p.m. to 12 a.m., lower right). Footprint contribution is shown as a color bar chart. Light blue dashed line is the shape footprint from numeric model to 95% contribution

and, consequently, the types of land use that most contribute to heat flux.

To further explore the collected datasets, we used simulated series of direction and wind speed of two grid points to assess uncertainties in shape and area of footprint derived by wind patterns. First grade point refers to Galeão International Airport meteorological gauge station ($43^{\circ} 14' 36.96''$ S, $22^{\circ} 48' 31.32''$ W) and the second to the center of the optical path ($43^{\circ} 14' 4.56''$ S, $22^{\circ} 51' 7.92''$ W). Simulated wind velocity has Pearson's correlation coefficients

of 0.63, and root mean square error (RMSE) of 1.34 ms^{-1} , when compared with measured wind at the Galeão Airport. Largest differences in wind pattern belong to wind direction. Both rose wind, from simulation and measurement are shown in Fig. 5. WRF simulations are able to capture the diurnal cycle of sea and land breeze at Galeão Airport (supplementary S.1). However, sea breeze is better represented by the model.

When simulated wind patterns at both locations are compared, Pearson's correlation coefficient is 0.91 for

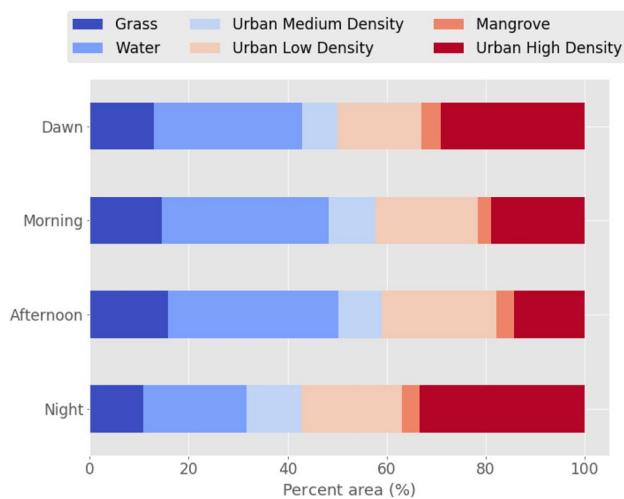


Fig. 4 Land-cover shares (grass, urban low density, urban medium density, urban high density, mangrove, and water) of the corresponding footprints for the four time periods along the day

wind speed. Differences between locations show a root mean square error (RMSE) of 0.64. Regarding simulated wind directions, both locations show the predominance of S–SE wind, characteristics of sea breeze events (Fig. 5). However, Ilha do Fundão show a larger frequency of S–W during the morning, which are also from the continent, and do not show E winds observed in Galeão Airport at night (S.1). Footprint model was also applied to the simulated wind at the center of the optical path, with the same model parameters previously used. The limits for the area corresponding to 95% of the contribution to the H flow were

demarcated and overlaid with the footprint areas generated from measured wind at Galeão Airport.

As expected, differences in wind speed drive differences in footprint area. However, footprint shape shows similar appearance during daytime periods, in which sea breeze dominates mesoscale wind patterns. Differences in the shape of the source areas are greatest in the afternoon and night. The advance of the contribution area over the continent during the night is not observed in the numerical results, as well as the advance in the western direction. It is important to highlight that WRF simulations of speed and wind direction are sensitive to the parameterization scheme adopted, which might generate a degree of uncertainty in the simulated wind field, as pointed out by Carvalho et al. 2014 and Gholami et al. 2021.

As Guimarães (2014) calls attention and reinforces by means of the wind spectral analysis performed using wavelets for the Guanabara Bay and surroundings based on different weather stations nearby, it is worthwhile to note that the MARJ is limited to the north-northwest by higher topography due to the Serra do Mar in Brazil, which regionally receives the name of Serra dos Órgãos. Therefore, it is acceptable to assume that the colder air that descends the mountain in the dawn and early morning reaches MARJ in the late morning and is associated with the previously established flow of the land breeze, causing intensification of the winds of the northern component.

3.3 Sensible heat flux

C_n^2 measurements ranged from 2.32×10^{-12} to $2.48 \times 10^{-11} \text{ m}^{-2/3}$ between December 16 and 22, 2017 and

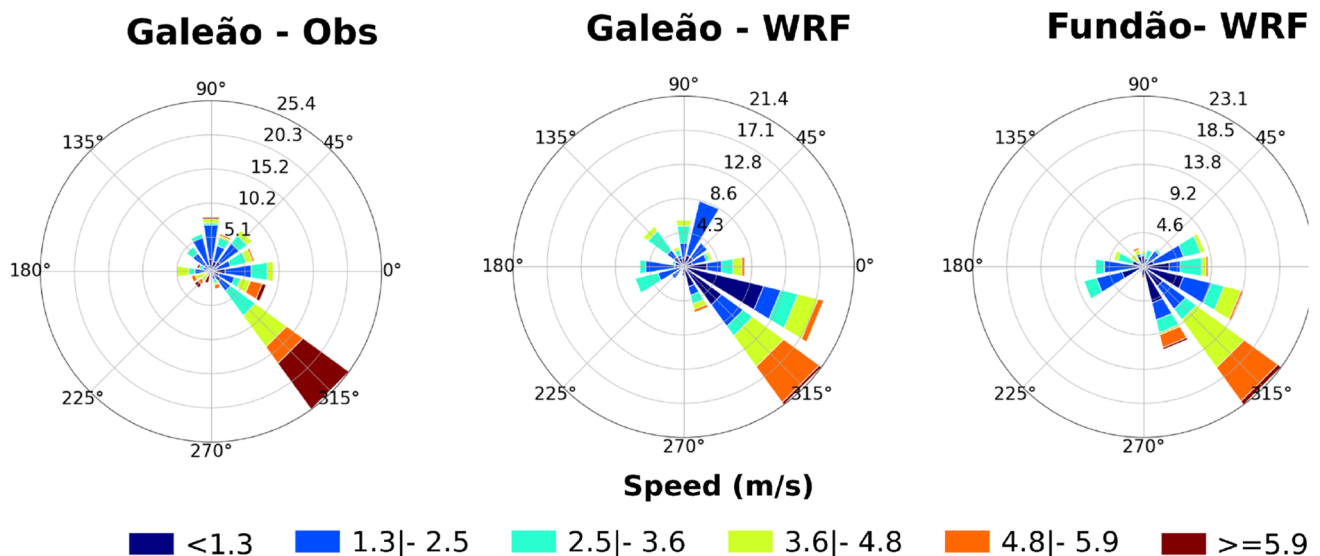
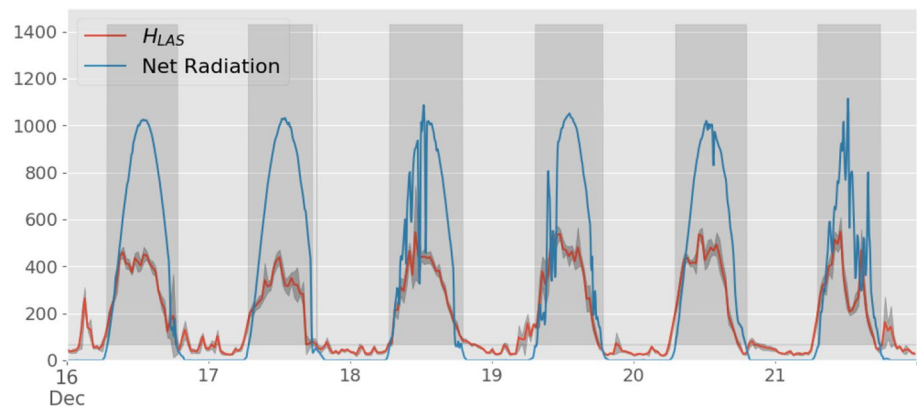
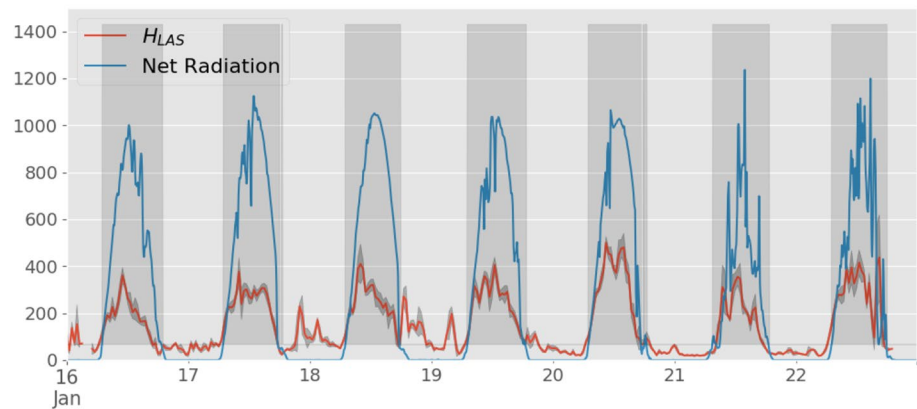


Fig. 5 Wind rose diagrams with the wind speed (ms^{-1}) frequency distribution broken down by wind direction for modeled values referring to Galeão and Ilha do Fundão (study location) and data observed at the Galeão weather station

Fig. 6 Sensible heat flux (Wm^{-2}) for December 16–22, 2017 (a) and January 16–22, 2018 (b). The red lines represent sensible heat flux (H_{LAS}) averaged via LAS over 30-min intervals. The shaded area is the standard-deviation value calculated over 30-min intervals. The blue line represents net radiation averaged over 5-min intervals. The dark bars correspond to unstable atmosphere conditions



(a) December 16 – 21, 2017



(b) January 16 – 22, 2018

2.03×10^{-12} to $8.19 \times 10^{-11} \text{ m}^{-2/3}$ from January 16 to 22, 2018. These values agree with the accepted threshold for saturation, as justified in the methodology previously presented. Diurnal H cycles follow an expected pattern based on arrival of solar and net radiation (Fig. 6). No rainfall was observed during these mostly clear-sky days, although the influence of cloud cover can be seen on December 18 and 21, 2017 and January on 21 and 22, 2018. Our study showed H responding consistently to changes in net radiation. Diurnal H variation shows a two-peak probability density function (Fig. 7). The smallest peak is related to atmosphere stability, while largest peaks are related to unstable atmosphere periods. On December 17, 2017 (Fig. 7a), the highest peak density was around 300 Wm^{-2} , while, in the other days, that value was higher. Lower air-specific humidity on December 17, 2017 could help explain that behavior (Fig. 2b). Higher air humidity values allow for greater latent heat fluxes compared to sensible heat fluxes. Similar behavior is also observed in January, 2018, in which lower sensible heat values were seen during days with higher air-specific humidity (Fig. 2b).

Despite differences in footprint area between morning and afternoon periods (Fig. 3b, c), averaged H values are similar because the rate between the area under each land use type and total footprint area remains similar (Fig. 4). During morning periods, when valley breeze is enhanced, H ranges from 19 to 594 Wm^{-2} , with an average value of 264 Wm^{-2} (Fig. 8a). Meanwhile, during afternoon periods, when sea breeze is predominant, H ranged from 32 to 589 Wm^{-2} , with an average value of 268 Wm^{-2} . The large number of outliers highlights the uncertainty of the free convection method for measuring stable atmosphere H (Fig. 8a).

Previous works show that the development of sea breeze tends to reduce sensible heat flow, as previously reported by Lee (2015), which was not observed in this research work. This behavior could be associated with the particular characteristics of the Fundão Island surroundings. In Fundão Island, the development of sea breeze drives heat advection from continental high-density urban areas (Fig. 4), which enhances the release of anthropogenic heat stored in buildings.

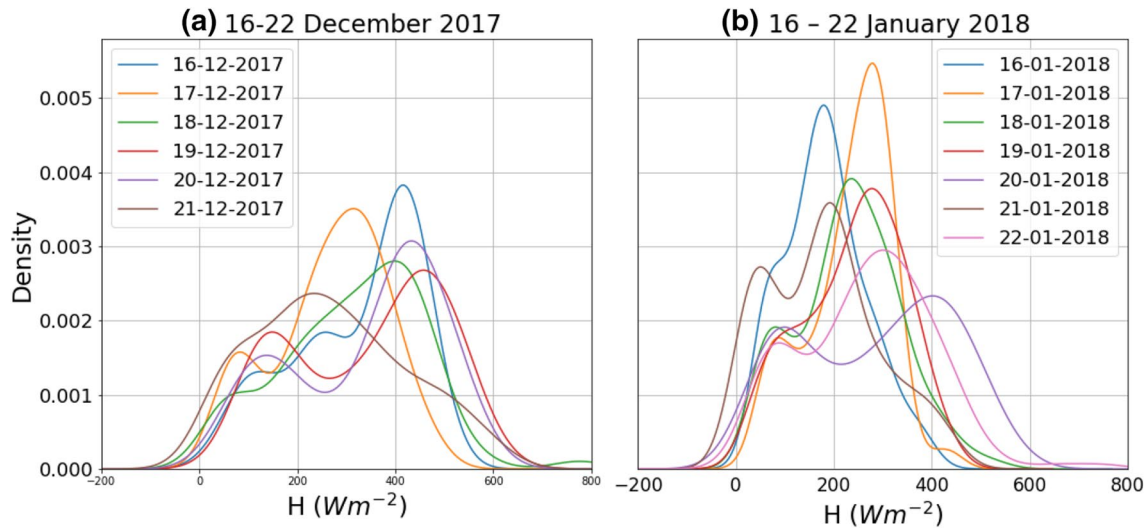


Fig. 7 Kernel density estimation of sensible heat flux (Wm^{-2}) for 16–22 December 2017 (a) and 16–22 January 2018 (b)

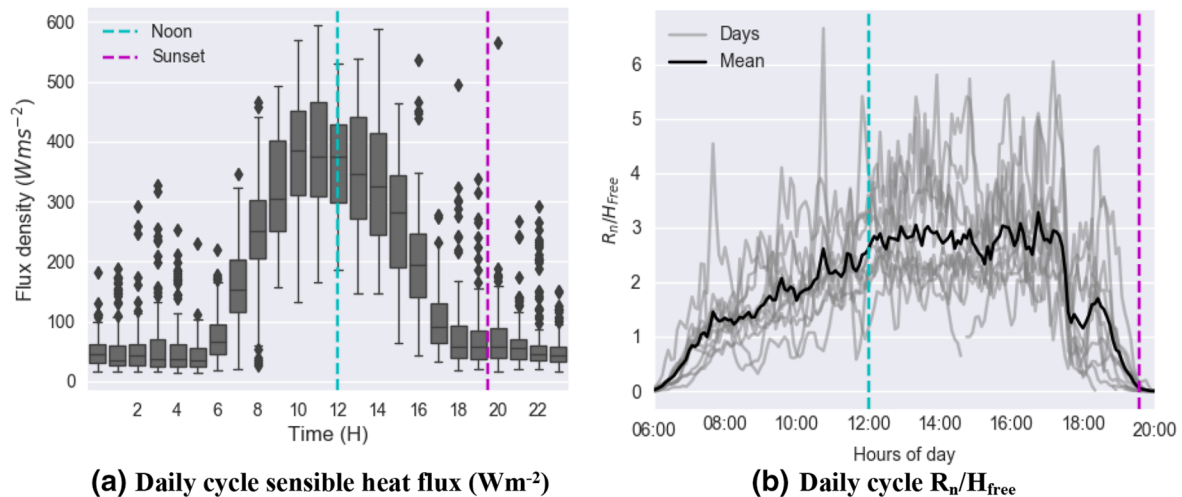


Fig. 8 Daily variation of sensible heat flux (H) (a) and R_n/H_{free} (b) along the days of the field experiment. The black line indicates the average for the days studied. The box plot in (a) indicates the range of variation for H values by hour of the day. The daily cycle of H

for each day evaluated for the experiment is shown in light gray lines in (b). The cyan line indicates the beginning of the afternoon period, wherein sea breeze regime influence occurs, while magenta line indicates the sunset

During the period studied, temperatures in the afternoon presented high values (Fig. 2a), while air-specific humidity was low (Fig. 2b), which helps to explain the high values of H . The low amplitude in the diurnal temperature cycle is characteristic of the tropical coastal area in which the Guanabara Bay is situated. Late afternoon depicted an abrupt reduction of H (Fig. 8b) due to the shading caused by topography, since, at the end of the afternoon, the Tijuca massif is positioned in the trajectory between the Sun and the Fundão island (Fig. 1). This result is consistent with the size of their footprints in the afternoon and early night periods, when larger values have been observed.

The ratio between net radiation (R_n) and H shows an upward trend (Fig. 8b) during mornings, reaching some stability after mid-day. During afternoon to early evening periods (2 p.m. to 6 p.m.), a fraction of storage heat discharge and heat emissions are manifested as H , resulting in an asymmetric decline of H related to the morning rise, similar to that found by Crawford et al. (2017). This hysteresis arrangement between R_n and H is recognized in the literature and presented in some studies (Monin and Yaglom 1981; Grimmond et al. 2004). Such relationship tends to be more evident on clear days, but it is not that obvious on partially cloudy or cloudy days (Ward et al. 2014).

3.4 Uncertainties in H estimate assessments

The LAS has a high sensitivity to fluctuations in H , which allows for the collection of very small time-scale data (< 60 min) (Kleissl et al. 2009). In this study, such robustness and reliability are evidenced in the dispersion identified with respect to H measurements retrieved from both evaluated time periods (Fig. 6). Dispersion tends to increase in diurnal times with higher H values, such as around mid-day. The uncertainties in H estimations conducted via LAS systems are magnified in stable conditions. On January 18 and 19, 2018, under stable conditions, H variations increase and mean values exceed the expected levels, reaching magnitudes higher than 200 W m^{-2} (Fig. 6b). It is possible that variations in atmospheric stability as altitude changes interfere with H estimates (Odhiambo and Savage 2009). On the other hand, it is important to note that the methodological approach used to determine stability conditions ($R_n < 50$, as described by Samain et al. 2012) does not consider the vertical profile of the atmosphere.

Sensitivity testing was conducted to quantify uncertainties related to the b constant (Eq. 4), effective height (z_{eff}), and air temperature (T) (Table 1). Higher and lower limits in a range of possible values were considered for each parameter. For parameter b , values of 0.474 (Andreas 1988) and 0.55 (Kohsiek 1982) were applied encompassing values used in previous published works. For z_{eff} , the lower and higher thresholds were 56.44 m and 62.44 m, based on uncertainties attributed to landscape complexity and occurrence of tides. Complementarily, possible uncertainties in the range of $\pm 10\%$ were considered for air temperature measurements.

Sensible heat flux estimations using the free method showed strong sensitivity to the empirical constant b and to effective height z_{eff} (Table 1). H estimates with the values of b obtained by Andreas (1988) and Kohsiek (1982) revealed differences of -16.8% and 3.4%, respectively. The

coefficients used in Andreas (1988) tend to underestimate H by 9–15% (Crawford et al. 2017). The result shows the high sensitivity of the method to constant b , in agreement with the results found in Lagouarde et al. (2005), which suggest that those uncertainties can reach values as high as 20%. Variations of $\pm 3.0 \text{ m}$ in z_{eff} resulted in a relative difference of 5.0% and 5.1% in H . This range covers the variation of high tide (1.27 m) and low tide (0.06 m) for the case study at hand, in addition to variations in zero-plane displacement (d). Lee et al. (2015) found uncertainties levels of $\pm 10\%$ in H estimates when z_{eff} changes by 11% due to the high influence of the diurnal tidal cycle. Considering a $\pm 10\%$ oscillation in the diurnal air temperature cycle (Fig. 2a), variations in the estimation of H were of 4.7% and 5.6%. This suggests that uncertainties in the estimation of the b parameter introduce larger dispersion in H estimates than potential errors in z_{eff} estimations or air temperature measurements.

4 Conclusion

Understanding the dynamics of heat exchanges on the Earth's surface is important for several scientific and technological areas. This work analyzed a series of sensible heat flux (H) measurements conducted via a large-aperture scintillometer in a complex urban landscape close to a bay surrounded by high topographic relief in the city of Rio de Janeiro, Brazil, during southern hemisphere summer. Land and sea breezes have an influence on the studied area. Such breezes caused a variation from 2.05 to 5.38 km^2 in the footprint area during the days of the experiment. The largest areas footprints were recorded during the afternoon and evening periods, when sea-breeze southeast (SE) winds were the prevailing force. However, due to the specific diurnal temperature cycle of this tropical coastal area, we did not observe a strong influence of sea breezes in the averaged LAS-estimated sensible heat flux values. On the other hand, the location of the study area relative to the higher topography and sun path movement leads to an abrupt decrease in sensible heat fluxes in the late afternoon. Scintillometry allows for a better understanding of how mesoscale atmospheric phenomenon influences the local dynamics of sensible flux in this complex region.

The footprint estimates could help develop and validate upscaling approaches such as the numerical estimation of pixel or grid-effective parameters used in land-surface models and remote-sensing-based products. The analysis of the daily variation of the source areas showed that the contribution of each type of land use varies throughout the day. Thus, for the understanding of the energy balance in urban coastal regions, as well as for the numerical modeling of these phenomena, it is important to consider this variation.

Table 1 Sensitivity tests for sensible heat flux (H)

	$H_{\text{sens}} (\text{W m}^{-2})$	Relative difference (%)
b		
0.474 (Andreas 1988)	139.0	- 16.8
0.55 (Kohsiek 1982)	161.4	- 3.4
LAS effective height (Z_{eff})		
56.44	158.7	- 5.0
62.44	175.6	5.1
Air temperature (T)		
+ 10%	176.5	5.6
- 10%	159.3	- 4.7

Relative difference was calculated by $(H_{\text{sens}} - H_{\text{base}})/H_{\text{base}} \times 100$, where H base (H_{base}) was estimated considering $z_{\text{eff}} = 59.44 \text{ m}$ and $b = 0.57$, resulting in average $H_{\text{base}} = 167.1 \text{ W m}^{-2}$

The results demonstrated the ability of LAS systems to acquire measurements at small time scales (less than 1 h) and its corresponding high sensitivity to fluctuations in air temperature and humidity, which influence the density distribution of H values. Also, uncertainties in wind measurements drive differences in shape and area of the footprint. Sensitivity testing showed that values of the empirical constant b can cause differences of up to 16%, in agreement with values found in former published literature. Variations in z_{eff} and air temperature caused relatively lower differences in H estimates.

Supplementary Information The online version contains supplementary material available at <https://doi.org/10.1007/s00703-021-00812-2>.

Acknowledgements Initially, the authors acknowledge the support of the Water Resources and Environmental Studies Laboratory (LABH2O) of the Civil Engineering Program (PEC) of the Alberto Luiz Coimbra Institute for Graduate Studies and Engineering Research (COPPE) and the Department of Meteorology from the Institute of Geosciences (IGEO), both institutes of the Federal University of Rio de Janeiro. Special thanks are directed to the support provided by the Rio de Janeiro Research Support Foundation (FAPERJ) in the form of financial resources through the projects. PEC/COPPE FAPERJ—Pensa Rio—Edital 34/2014 (2014–2018)—E-26/010.002980/2014, FAPERJ Emergencial E_12/2015 (2015–2017)—processo E-26-203.535/2015, CNPq Edital Universal No. 14/2013 (2013–2017)—processo 485136/2013-9, CNPq Edital Universal No. 28/2018—processo 435714/2018-0, CNPq—Edital No. 12/2016—processo 306944/2016-2, CNPq Edital No. 09/2018—processo 308358/2018-0 and CNPq Edital No 06/2019—processo 303846/2019-4. Finally, the authors would like to recognize that this study was financed in part by Coordenação de Aperfeiçoamento de Pessoal de Nível Superior—Brasil (CAPES) —Finance Code 001.

References

- Airbus D&S (2015) WorldDEM Technical Product Specification. Data-sheet, Toulouse
- Al-Gaadi KA, Patil VC, Tola E, Madugundu R, Gowda PH (2016) Evaluation of METRIC-derived ET fluxes over irrigated alfalfa crop in desert conditions using scintillometer measurements. *Arab J Geosci* 9:441–452
- Andreas EL (1988) Estimating C_n2 over snow and sea ice from meteorological data. *J Opt Soc Am A* 5:481–495
- Anjos M, Lopes A (2019) Sea breeze front identification on the northeastern coast of Brazil and its implications for meteorological conditions in the Sergipe region. *Theor Appl Climatol* 137:2151–2165
- Becek K, Koppe W, Kutoğlu ŞH (2016) Evaluation of vertical accuracy of the WorldDEMTM using the runway method. *Remote Sens* 8:934–946
- Boselli A, Armenante M DL, D'Isidoro M, Pisani G, Spinelli N, Wang X (2009) Atmospheric aerosol characterization over Naples during 2000–2003 EARLINET project: planetary boundary-layer evolution and layering. *Boundary-Layer Meteorol* 132:151–165
- Carvalho D, Rocha A, Gómez-Gesteira M, Silva Santos C (2014) Sensitivity of the WRF model wind simulation and wind energy production estimates to planetary boundary layer parameterizations for onshore and offshore areas in the Iberian Peninsula. *Appl Energy* 135:234–246
- Chehbouni A, Kerr YH, Watts C, Hartogensis O, Goodrich D, Scott R, Schiedge J, Lee K, Shuttleworth WJ, Dedieu G, De Bruin HAR (1999) Estimation of area-average sensible heat flux using a large-aperture scintillometer during the Semi-Arid Land-Surface-Atmosphere (SALSA) Experiment. *Water Resour Res* 35:2505–2511
- Crawford B, Grimmond CSB, Ward HC, Morrison W, Kotthaus S, Crawford B (2017) Spatial and temporal patterns of surface – atmosphere energy exchange in a dense urban environment using scintillometry. *Quart J Royal Meteorol Soc* 237:817–833
- Crawford B, Grimmond CSB, Gabey A, Marconcini M, Ward HC, Kent CW (2018) Variability of urban surface temperatures and implications for aerodynamic energy exchange in unstable conditions. *Quart J R Meteorol Soc* 144:1719–1741
- Da Silva FP, Filho OCR, Sampaio RJ, Cunha I, Dragaud ICDV, Araújo AMA, Justi MGA, Dornelles G (2017) Evaluation of atmospheric thermodynamics and dynamics during heavy - rainfall and no - rainfall events in the metropolitan area of Rio de Janeiro, Brazil. *Meteorol Atmos Phys*. <https://doi.org/10.1007/s00703-017-0570-5>
- De Bruin HAR (1995) The scintillation method tested over a dry vineyard area. *Bound-Layer Meteorol* 76:25–40
- De Tomasi F, Miglietta MM, Perrone MR (2011) The growth of the planetary boundary layer at a coastal site: a case study. *Boundary-Layer Meteorol* 139:521–541
- de Júnior JFO, Cristina J, Souza S, Dias FO, Gois G, Frederico I, Gonçalves S, Soares M (2013) Caracterização do Regime de Vento no Município de Seropédica, Rio de Janeiro (2001–2010) Characterization of Wind Regime in Seropédica. *Floresta e Ambiente* 20:447–459
- de Júnior JFO, de Terassi PMB, de Gois G (2018) Estudo Da Circulação Dos Ventos Na Baía De Guanabara/Rj, Entre 2003 E 2013. *Rev Bras Climatol* 21:59–80
- de Peres LF, de Lucena AJ, Rotunno Filho OC, de França JRA (2018) The urban heat island in Rio de Janeiro, Brazil, in the last 30 years using remote sensing data. *Int J Appl Earth Obs Geoinf* 64:104–116
- Dragaud ICDV, Soares da Silva M, de Assad LPF, Cataldi M, Landau L, Elias RN, Pimentel LCG (2018) The impact of SST on the wind and air temperature simulations: a case study for the coastal region of the Rio de Janeiro state. *Meteorol Atmos Phys*. <https://doi.org/10.1007/s00703-018-0622-5>
- Dudhia J (1989) Numerical study of convection observed during the winter monsoon experiment using a mesoscale two-dimensional model. *J Atmos Sci* 46:3077–3107
- Ezzahar J, Chehbouni A, Hoedjes JCB, Er-Raki S, Chehbouni A, Boulet G, Bonnefond JM, De Bruin HAR (2007a) The use of the scintillation technique for monitoring seasonal water consumption of olive orchards in a semi-arid region. *Agric Water Manag* 89:173–184
- Ezzahar J, Chehbouni A, Hoedjes JCB, Chehbouni A (2007b) On the application of scintillometry over heterogeneous grids. *J Hydrol* 334:493–501
- Grimmond CSB, Salmond JA, Oke TR, Offerle B, Lemonsu A (2004) Flux and turbulence measurements at a densely built-up site in Marseille: Heat, mass (water and carbon dioxide), and momentum. *J Geophys Res D Atmos* 109:1–19. <https://doi.org/10.1029/2004JD004936>
- Gholami S, Ghader S, Khaleghi-Zavareh H, Ghafarian P (2021) Sensitivity of WRF-simulated 10 m wind over the Persian Gulf to different boundary conditions and PBL parameterization schemes. *Atmos Res* 247:105147–105165
- Giannaros TM, Kotroni V, Lagouvardos K, Dellis D, Tsanakas P, Mavrellis G, Symeonidis P, Vakkas T (2017) Ultrahigh resolution wind forecasting for the sailing events at the Rio de Janeiro 2016 Summer Olympic Games. *Meteorol Appl* 25:86–93
- Giannaros C, Nenes A, Giannaros TM, Kourtidis K, Melas D (2018) A comprehensive approach for the simulation of the Urban Heat

- Island effect with the WRF/SLUCM modeling system: the case of Athens (Greece). *Atmos Res* 201:86–101
- Goldreich Y, Druyan LM, Berger H (1986) The interaction of valley/mountain winds with a diurnally veering sea/land breeze. *J Climatol* 6:551–561
- Guimarães JM (2014) Circulações locais na Região Metropolitana do Rio de Janeiro: Aspectos observacionais, MSc Thesis, Civil Engineering Program, COPPE, Federal University of Rio de Janeiro
- Haeger-Eugensson M (1999) Vertical interactions in a nocturnal multi-scale wind system influenced by atmospheric stability in a coastal area. *Theor Appl Climatol* 64:69–82
- Hartogensis OK, Rodriguez JC, Watts CJ, Rodriguez JC, Bruin HAR (2003) Derivation of an effective height for scintillometers: La Poza experiment in Northwest Mexico. *J Hydrometeorol* 4:915–928
- Hemakumara HM, Chandrapala L, Moene AF (2003) Evapotranspiration fluxes over mixed vegetation areas measured from large aperture scintillometer. *Agric Water Manag* 58:109–122
- Hill RJ, Lataitis RJ (1989) Effect of refractive dispersion on the trichromatic correlation of irradiances for atmospheric scintillation. *Appl Opt* 28:4121–4125
- Hoedjes JCB, Chehbouni A, Ezzahar J, Escadafal R, De Bruin HAR (2007) Comparison of Large Aperture Scintillometer and Eddy Covariance Measurements: Can Thermal Infrared Data Be Used to Capture Footprint-Induced Differences? *J Hydrometeorol* 8:144–159. <https://doi.org/10.1175/JHM561.1>
- Hong S-Y, Dudhia J, Chen S-H (2004) A revised approach to ice microphysical processes for the bulk parameterization of clouds and precipitation. *Mon Weather Rev* 132:103–120
- Hong SY, Noh Y, Dudhia J (2006) A new vertical diffusion package with an explicit treatment of entrainment processes. *Mon Weather Rev* 134:2318–2341
- Iamarino M, Beevers S, Grimmond CSB (2012) High-resolution (space, time) anthropogenic heat emissions: London 1970–2025. *Int J Climatol* 32:1754–1767
- Imukova K, Ingwersen J, Streck T (2015) Determining the spatial and temporal dynamics of the green vegetation fraction of croplands using high-resolution RapidEye satellite images. *Agric for Meteorol* 206:113–123
- Ingwersen J, Steffens K, Högy P, Warrach-Sagi K, Zhunusbayeva D, Poltoradnev M, Gäbler R, Wizemann HD, Fangmeier A, Wulfmeyer V, Streck T (2011) Comparison of Noah simulations with eddy covariance and soil water measurements at a winter wheat stand. *Agric for Meteorol* 151:345–355
- Jiménez PA, Dudhia J, González-Rouco JF, Navarro J, Montávez JP, García-Bustamante E (2012) A revised scheme for the WRF surface layer formulation. *Mon Weather Rev* 140:898–918
- Jiménez-Esteve B, Udina M, Soler MR, Pepin N, Miró JR (2018) Land use and topography influence in a complex terrain area: a high resolution mesoscale modelling study over the eastern pyrenees using the WRF model. *Atmos Res* 202:49–62
- Kleissl J, Watts CJ, Rodriguez JC, Naif S, Vivoni ER (2009) Scintillometer intercomparison study—continued. *Boundary-Layer Meteorol* 130:437–443
- Klessl J, Hong SH, Hendrickx MH (2009) New Mexico scintillometer network: supporting remote sensing and hydrologic and meteorological models. *Bull Am Meteorol Soc* 90:207–218
- Kohsiek W (1982) Measuring Ct_2 , Cq_2 , and Ct_q in the unstable surface layer, and relations to the vertical fluxes of heat and moisture. *Boundary-Layer Meteorol* 24(24):89–107
- Kormann R, Meixner FX (2000) An analytical footprint model for non-neutral stratification. *Boundary-Layer Meteorol* 99:207–224
- Lagouarde JP, Irvine M, Bonnefond CSB, Grimmond CSB, Long N, Oke TR, Salmund JA, Offerle B (2005) Monitorin the sensible heat flux over urban areas using large aperture scintillometry: case study of marseille city during the escompte experiment. *Bound-Layer Meteorol* 18:449–476
- Lee SH (2015) Determination of turbulent sensible heat flux over a coastal maritime area using a large aperture scintillometer. *Bound-Layer Meteorol* 157:309–319
- Lee SH, Kim SW, Angevine WM, Bianco L, McKeen SA, Senff CJ, Trainer M, Tucker SC, Zamora RJ (2011) Evaluation of urban surface parameterizations in the WRF model using measurements during the Texas Air Quality Study 2006 field campaign. *Atmos Chem Phys* 11:2127–2143
- Lee S-H, Lee J-H, Kim B-Y (2015) Estimation of turbulent sensible heat and momentum fluxes over a heterogeneous urban area using a large aperture scintillometer. *Adv Atmos Sci* 32:1092–1105
- Liu SM, Xu ZW, Wang WZ, Jia ZZ, Zhu MJ, Bai J, Wang JM (2011) Sciences A comparison of eddy-covariance and large aperture scintillometer measurements with respect to the energy balance closure problem. *Hydrol Earth Syst Sci* 15:1291–1306
- Liu SM, Xu ZW, Zhu ZL, Jia ZZ, Zhu MJ (2013) Measurements of evapotranspiration from eddy-covariance systems and large aperture scintillometers in the Hai River Basin, China. *J Hydrol* 487:24–38
- Liu X, Li X, Harshan S, Roth M, Velasco E (2017) Evaluation of an urban canopy model in a tropical city: the role of tree evapotranspiration. *Environ Res Lett* 12:94008–94020
- Liu X, Tian G, Feng J, Ma B, Wang J, Kong L (2018) Modeling the warming impact of urban land expansion on hot weather using the weather research and forecasting model: a case study of Beijing, China. *Adv Atmos Sci* 35:723–736
- Masson V (2000) A physically-based scheme for the urban energy. *Boundary-Layer Meteorol* 94:357–397
- Meijninger WML, Hartogensis OK, Kohsiek W, Hoedjes JCB, Zuurbier RM, Bruin HHR (2002) Determination of area-averaged sensible heat fluxes with a large aperture scintillometer over. *Bound-Layer Meteorol* 105:37–62
- Melas D, Kambezidis HD (1992) The depth of the internal boundary layer over an urban area under sea-breeze conditions. *Boundary-Layer Meteorol* 61:247–261
- Mestayer PG, Durand P, Augustin P, Bastin S (2005) The Urban Boundary-layer Field Campaign In Marseille (Ubl / Clu-escompte): Set-up And First Results 1. Introduction The assessment of air quality within an urban area requires that numerical models be able to simulate pollutant transport-diffusion and. *Boundary-Layer Meteorol* 114:315–365
- Minacapilli M, Cammalleri C, Ciraolo G, Rallo R, Provenzano G (2016) Using scintillometry to assess reference evapotranspiration methods and their impact on the water balance of olive groves. *Agric Water Manag* 170:49–60
- Mlawer EJ, Taubman SJ, Brown PD, Iacono MJ, Clough SA (1997) Radiative transfer for inhomogeneous atmosphere: RRTM, a validated correlated-k model for the longwave. *J Geophys Res* 102:16663–16682
- Monin and Yaglom (1981) Statistical fluid mechanics: mechanics of turbulence (Volume 2). Cambridge Univ Press. <https://doi.org/10.1109/ICDAR.2011.95>
- Moene AF (2003) Effects of water vapour on the structure parameter of the refractive index for near-infrared radiation. *Bound-Layer Meteorol* 107:635–653
- Naor R, Potchter O, Shafir H, Alpert P (2017) An observational study of the summer Mediterranean Sea breeze front penetration into the complex topography of the Jordan Rift Valley. *Theor Appl Climatol* 127:275–284
- Ochs GR, RJ Hill (1982) A study of factors influencing the calibration of optical meters. NOAA Tech. Memo. ERL WPL-106. National Technical Information Service. Springfield
- Odhiambo GO, Savage MJ (2009) Surface layer scintillometry for estimating the sensible heat flux component of the surface energy balance. *S Afr J Sci* 105:208–216
- Oke TR (1987) Boundary layer climates. Routledge, New York

- Oke TR (2004) Initial guidance to obtain representative meteorological observations at urban sites. Instruments and Methods of Observation Program. REPORT, New York
- Oke TR, Mills G, Christen A, Voogt JA (2017) Urban Climates. Cambridge University Press, Cambridge
- Papangelis G, Tombrou M, Dandou A, Kontos T (2012) An urban “green planning” approach utilizing the Weather Research and Forecasting (WRF) modeling system. A case study of Athens. *Greece Landsc Urban Plan* 105:174–183
- Paranhos BR, Rangel RHO, de Sá RV, Cataldi M (2019) Wind power use capacity in rural areas of complex topography via WRF model: a case study in a mountainous region in Rio de Janeiro state, Brazil. *Anu Do Inst Geociencias* 42:52–63. https://doi.org/10.11137/2019_3_52_63
- Pigeon G, Lemonsu A, Grimmond CSB, Durand P, Thouron O, Masson V (2007) Divergence of turbulent fluxes in the surface layer: case of a coastal city. *Boundary-Layer Meteorol* 124:269–290
- Pimentel LCG, Marton E, da Silva MS, Jourdan P (2014) Caracterização do regime de vento em superfície na Região Metropolitana do Rio de Janeiro. *Eng Sanit e Ambient* 19:121–132
- Román-Cascón C, Yagüe C, Mahrt L, Sastre M, Steeneveld GJ, Pardyjak E, Van De Boer A, Hartogensis O (2015) Interactions among drainage flows, gravity waves and turbulence: a BLLAST case study. *Atmos Chem Phys* 15:9031–9047
- Samain B, Defloor W, Pauls VRN (2012) Continuous time series of catchment-averaged sensible heat flux from a large aperture scintillometer: efficient estimation of stability conditions and importance of fluxes under stable conditions. *Am Meteorol Soc* 13:423–442
- Sicard M, Pérez C, Rocadenbosch F, Baldasano FM, García-Vizcaino D (2006) Mixed-layer depth determination in the barcelona coastal area from regular lidar measurements: methods results and limitations. *Boundary-Layer Meteorol* 119:135–157
- Skamarock WC, Klemp JB, Dudhi J, Gill DO, Barker DM, Duda MG, Huang X-Y, Wang W, Powers JG (2008) A Description of the Advanced Research WRF Version 3. NCAR Technical Note NCAR/TN-475+STR. Tech Rep 113. New York
- Soares-Gomes A, da Gama BAP, Baptista Neto JA, Freire DG, Cordeiro RC, Machado W, Bernardes MC, Coutinho R, Thompson FL, Pereira RC (2016) An environmental overview of Guanabara Bay, Rio de Janeiro. *Reg Stud Mar Sci* 8:319–330
- Sobral BS, de Oliveira Júnior JF, de Gois G, Terassi PM de B, Pereira CR (2018) Wind regime in Serra do Mar Ridge-Rio de Janeiro, Brazil. *Rev Bras Meteorol* 33:441–451. <https://doi.org/10.1590/0102-7786333004>
- Stull RB (1988) An introduction to boundary layer meteorology. Springer Science & Business Media, Dordrecht
- Sun G, Hu Z, Sun F, Wang J, Xie Z, Lin Y, Huang F (2016) An analysis on the influence of spatial scales on sensible heat fluxes in the north Tibetan Plateau based on Eddy covariance and large aperture scintillometer data. *Theor Appl Climatol* 129:965–976
- Sun X, Holmes H, Osibanjo O, Sun Y, Ivey C (2017) Evaluation of surface fluxes in the WRF model: case study for farmland in rolling terrain. *Atmosphere (basel)* 8:197–220
- Tatarskiĭ V (1961) Wave propagation in a turbulent medium. McGraw-Hill, USA
- Tewari M, Chen F, Kusaka H, Miao S (2007) Coupled WRF/Unified Noah/Urban-Canopy Modeling System. NCAR WRF Documentation 1:1–20
- Thiermann V, Grassl H (1992) The measurement of turbulent surface-layer fluxes by use of bichromatic scintillation. *Bound-Layer Meteorol* 58:367–389
- Valayamkunnath P, Sridhar V, Zhao W, Allen RG (2018) Intercomparison of surface energy fluxes, soil moisture, and evapotranspiration from eddy covariance, large-aperture scintillometer, and modeling across three ecosystems in a semiarid climate. *Agric for Meteorol* 248:22–47
- Vázquez DM, Ramamurthy P, Arend M, González-Cruz JE (2018) Thermal structure of a coastal-urban boundary layer. *Boundary-Layer Meteorol* 169:151–161
- Villela RJ (2018) The South Atlantic convergence zone: a critical view and overview. *Rev Do Inst Geológico* 38:1–19
- Von Randow C, Kruijt B, Holtslag AAM, Oliveira de MB (2008) Exploring eddy-covariance and large-aperture scintillometer measurements in an Amazonian rain forest. *Agric for Meteorol* 148:680–690
- Von Randow RCS, Von RC, Hutjes RWA, Tomasella J, Kruijt B (2012) Evapotranspiration of deforested areas in central and southwestern Amazonia. *Theor Appl Climatol* 109:205–220
- Ward HC, Evans JG, Grimmond CSB (2014) Multi-scale sensible heat fluxes in the suburban environment from large-aperture scintillometry and Eddy covariance. *Boundary-Layer Meteorol* 152:65–89
- Watts CJ, Chehbouni A, Rodriguez JC, Kerr YH, Hartogensis O, De Bruin HAR (2000) Comparison of sensible heat flux estimates using AVHRR with scintillometer measurements over semi-arid grassland in northwest Mexico. *Agric for Meteorol* 105:81–89
- Wesely M (1976) The combined effect of temperature and humidity fluctuations on refractive index. *J Appl Meteorol* 15:43–49
- Xu Z, Liu S, Li X, Shi S, Wang J, Zhu Z, Xu T, Wang W, Ma M (2013) Intercomparison of surface energy flux measurement systems used during the HiWATER-MUSOEXE. *J Geophys Res Atmos* 118:13140–13157
- Xu F, Wang W, Wang J, Xu Z, Qi Y, Wu Y (2017) Area-averaged evapotranspiration over a heterogeneous land surface: aggregation of multi-point EC flux measurements with a high-resolution land-cover map and footprint analysis. *Hydrol Earth Syst Sci* 21:4037–4051
- Yee MS, Pauwels VRN, Daly E, Beringer J, Rüdiger C, McCabe MF, Walker JP (2015) A comparison of optical and microwave scintillometers with eddy covariance derived surface heat fluxes. *Agric for Meteorol* 213:226–239
- Zeng F, Gao N (2017) Use of an energy balance model for studying urban surface temperature at microscale. *Procedia Eng* 205:2956–2966
- Zeri M, Oliveira-Júnior JF, Lyra GB (2011) Spatiotemporal analysis of particulate matter, sulfur dioxide and carbon monoxide concentrations over the city of Rio de Janeiro, Brazil. *Meteorol Atmos Phys* 113:139–152
- Zhang H, Zhang H (2014) Comparison of turbulent sensible heat flux determined by large-aperture scintillometer and eddy covariance over urban and suburban areas. *Bound-Layer Meteorol* 154:119–136
- Zhao W, Zhang N, Sun J, Zou J (2014) Evaluation and parameter-sensitivity study of a single-layer urban canopy model (SLUCM) with measurements in Nanjing, China. *J Hydrometeorol* 15:1078–1090
- Zhao J, Olivas PC, Kunwor S, Malone SL, Staudhammer CL, Starr G, Oberbauer SF (2018) Comparison of sensible heat flux measured by large aperture scintillometer and eddy covariance in a seasonally-inundated wetland. *Agric for Meteorol* 259:345–354
- Zieliński M, Fortuniak K, Pawlak W, Siedlecki M (2013) Turbulent sensible heat flux in Łódź, Central Poland, obtained from scintillometer and eddy covariance measurements. *Meteorol Z* 22:603–613
- Zieliński M, Fortuniak K, Pawlak W, Siedlecki M (2018) Long-term turbulent sensible-heat-flux measurements with a large-aperture scintillometer in the Centre of Łódź, Central Poland. *Boundary-Layer Meteorol* 167:469–492